ORIGINAL ARTICLE

The Effect of Porosity, Oxygen and Phase Morphology on the Mechanical Properties of Selective Laser Melted Ti-6Al-4V with Respect to Annealing Temperature

A. Sai Deepak Kumar[1] · Deepak K. Pattanayak[2,3] · Mohammad Fayaz Anwar[1] · Archana Rajendran[2,3] · C. Vanitha[1]

Abstract In the present study, Ti-6Al-4V alloy was fabricated by Selective Laser Manufacturing (SLM) technique and subsequently subjected to an annealing treatment at, above and below the β transition temperature. We emphasized the influence of porosity, oxygen and phase morphology on the strength, ductility and elongation of SLM-manufactured Ti-6Al-4V and compared the alloy's properties with conventionally manufactured Ti-6Al-4V from the literature. The as-built Ti-6Al-4V sample showed a very high strength due to acicular martensite, and the growth of α+β lamellae on heat treatment improved ductility. Energy Dispersive Spectroscopy (EDS), Optical and Scanning Electron Microscopy (SEM) were used to identify the chemical composition, calculate lamellar width and analyze the fracture mechanisms. The grain size and the average thickness of α lamellae, inter-granular β and prior β grain boundary increased with annealing temperature. The porosity and oxygen content of the samples were found to have a consequential effect on the strength, especially in as-built and high-temperature annealing conditions and optimum mechanical properties were observed in SLM Ti-6Al-4V annealed at 800 °C.

Keywords Ti-6Al-4V · Selective laser melting · Annealing · Phase morphology · Porosity · Oxidation

✉ A. Sai Deepak Kumar
  sayyalasomayajula@student.nitw.ac.in

✉ Deepak K. Pattanayak
  deepak@cecri.res.in

✉ C. Vanitha
  vanitha@nitw.ac.in

  Mohammad Fayaz Anwar
  amohammadfayaz@student.nitw.ac.in

  Archana Rajendran
  archanaraj89@gmail.com

1 Department of Metallurgical and Materials Engineering, National Institute of Technology Warangal, Telangana 506004, India

2 CSIR-Central Electrochemical Research Institute, Karaikudi, Tamil Nadu 630006, India

3 Academy of Scientific and Innovative Research (AcSIR), Ghaziabad 201002, India

1 Introduction

The manufacturing of Ti-6Al-4V has always been challenging due to its poor thermal conductivity, ease of strain hardening and chemical reactivity with oxygen [1]. Conventional manufacturing involves a high amount of material loss in the form of processing waste, high manufacturing costs and several intermittent processing steps that increase the time for manufacturing a single part. Though conventionally manufactured Ti-6Al-4V is used in compressor blades of gas turbines, the processing costs involved are very high due to the poor machinability of Ti-6Al-4V, its susceptibility to weld with machining tools and increasing temperatures at the tool-sample interface. Considerable efforts made to improve the machining process such as the use of cryogenics like LN_2 and CO_2 [2, 3], WC cutting tool [4], Minimum Quantity Lubrication [5] and EDM [6], only increase the overall cost in the fabrication of Ti-6Al-4V with good surface finish. Due to this, the demand for cost-effective alternative manufacturing processes that produce defect-free, high-precision, quality parts and improve the high-temperature strength of the alloy without the need for further processing is increasing today. Additive Manufacturing (AM) is one such near-net shape process that is cost-effective mainly due to the low "buy-to-fly" ratio of the printed parts [7, 8]. AMed Ti-6Al-4V has been extensively studied in recent years and

used widely in biomedical, automobile and aerospace fields. Techniques such as Selective Laser Melting (SLM), Electron Beam Melting (EBM), Laser Metal Deposition (LMD) and Directed Energy Deposition (DED) in AM produce high-strength Ti-6Al-4V alloys. Li N. et al. discussed the variation of ultimate tensile strength, ductility and anisotropy with processing routes LMD and DED [9]. In all the above processes, a laser or electron beam melts the feed metallic powder, creating a molten pool which solidifies rapidly. The cooling rate has a profound effect on the as-fabricated Ti-6Al-4V structure [10–12]. Maly M. et al. preheated the powered bed over a range from 200 to 500 °C and observed the temperature effect on the residual stress, oxygen content and top-surface distortion [13].

In Ti-6Al-4V, the rapid cooling of the melt pool leads to $\alpha^{'}$ martensitic structure. This structure results in very poor ductility and a large accumulation of thermal and residual stresses, which contribute to defects such as cracks or pores. The presence of large pores renders the alloy futile for biological and aerospace applications. Hence, the fabricated parts are often heat treated at various temperatures above or below the β transus temperature (~ 995 °C) depending on the desired properties. Al-Rubaie et al. carried out annealing on the as-fabricated SLM Ti-6Al-4V at 675 °C for 1 h in the vacuum followed by slow cooling at a rate below 2.5 °C/min to obtain optimum strength and ductility [14].

Alternatively, the process parameters and environment are also controlled to change the microstructure in the as-fabricated condition and, consequently, the mechanical properties. The build direction of the sample can significantly affect the prior β grain size. Simonelli et al. reported this grain size variation along the edge, frontal and lateral planes and observed high ductility and good strength in the edge orientation [15]. Further, the inert gas atmosphere of the traditional SLM was replaced by vacuum by Zhou et al. [16] to avoid any entrapment of inert gas in the Ti-6Al-4V lattice. Liu L. et al. [17] introduced 5% vol N_2 with Ar during the SLM process, and the martensite formed was found to be wider than in the case of pure Ar atmosphere. Further, the martensite decomposed as N_2 dissolved in Ti64, contributing to increased elongation and strength, respectively, with laser power. The martensite size also increases with an increase in hatch spacing until a certain value of scanning velocity and then decreases for a given energy density, providing an opportunity to control the as-built microstructure [18]. With an increase in laser energy input, the susceptibility to form denser and larger martensite lath (and hence harder) Ti64 increases at the cost of surface roughness [19]. Xu W. et al. and Liu J. et al. achieved high strength and ductility by enabling the in-situ decomposition of martensite and restricting its formation, respectively, through controlling SLM parameters [11, 20]. Additionally, they correlated the volume fraction of martensite with laser power/energy

density and its impact on the alloy's mechanical properties and fracture. Song B. et al. developed a 3D Finite Element Model to understand the temperature distribution and molten pool depth and produced dense 3D parts with a laser power of 110W and a scan rate of 110 m/s [21]. Further increase in scan rate would lead to exacerbated porosity in the sample. The cooling rate during SLM is directly contingent upon laser power and scanning speed. High scanning speed decreases the heat input per unit length and increases the temperature gradient leading to a high cooling rate. On the contrary, an increase in laser power at a fixed scanning speed increases heat input and the size of the molten pool and decreases the cooling rate, which was investigated by Manvatkar V. et al., using three-dimensional heat transfer and flow models [22]. Residual stress in the as-built sample is another parameter that severely influences the as-fabricated morphology. Low laser power and high sample exposure time will result in lower residual stress and higher elongation due to an increase in α lath size because of the low cooling rate involved. Sun et al. implemented the Taguchi method to optimize the SLM parameters and arrived at a regression relation between density, laser power, scanning speed, powder thickness and scanning strategy [23]. Shi X. et al. achieved a 99.99% dense Ti64 using high layer thickness and coarse initial powders with mechanical properties comparable to alloys manufactured with small layers and fine powder, which has the potential to reduce the cost of SLM [24]. The scan strategy during SLM also plays a crucial role in deciding the fraction of α lath boundaries and local microstructure, which was clearly explained by Shao M. [25]. Notwithstanding many advantages, the biggest challenges faced in powder processing using AM are defects and anisotropy. Gong H. et al. elucidated the various factors affecting the formation of defects and their consequences on the strength, ductility and fracture mechanism [26, 27].

Most of the existing literature is pertaining to the low-temperature annealing effects, and none of the studies emphasized the combined impact of defects, high-temperature annealing, oxygen, porosity, unmelted particles, grain size and lamellar morphology and connected with the mechanical properties of Ti64 alloy processed through SLM. Hence in the present study, an effort has been taken to understand the above parameters and correlate them with the mechanical properties of the high-temperature annealed SLMed Ti64 alloy.

2 Material and Methods

2.1 Material Processing

Ti-6Al-4V powder (Grade 5) with an average particle size of 45~63 μm was used to fabricate samples. The powder

particles were produced by the gas atomization process and were spherical in shape. The chemical composition is given in Table 1.

Ti-6Al-4V samples of dimension 10 mm × 10 mm × 10 mm were built using the Selective Laser Melting (SLM) process (EOS M290 model, Germany). Nd: YAG laser was used to melt the powder in the presence of Ar atmosphere. The samples were produced with a laser power of 225W, a scanning speed of 600 mm/s, 50 µm hatch distance and a layer thickness of 40 µm. The powder bed was preheated to a temperature of 165 °C. The laser followed a zigzag pattern with a rotation angle of 67°. This angle was selected to get the maximum possible rotations between laser tracks with identical orientations. The SLM printed samples were annealed in a vertical tubular furnace under a vacuum of 10^{-3} bar. Annealing was carried out with a heating rate of 5 °C /min, and the samples were annealed and soaked for 2 h at four different temperatures, i.e., 800 °C, 1000 °C, 1200 °C, 1400 °C and furnace cooled.

2.2 Density Measurement

The density of the annealed Ti-6Al-4V samples was measured using Archimedes' principle.

2.3 Metallography

All the samples were polished using emery papers of 1/0 to 4/0 grade on the cross-section perpendicular to build direction and later on disc polisher. These samples were observed under Optical Microscope (OM), Model: QUASMO Qmm 500, after etching for 30 seconds with 46 mL H_2O + 6 mL HNO_3 + 3–6 mL HF. The average grain size was measured using the line intercept method as per ASTM E112. Scanning Electron Microscope (SEM, Model: TESCAN, Vega 3

LMU) was also used for observation. The average α lamellar thickness, prior β boundary thickness and thickness of the inter-granular β phase were measured for all the samples. Analysis of pores, unmelted particles and the whole sample was carried out under SEM to identify the morphology. Energy Dispersive Spectroscopy (EDS) was used to check if there was any oxidation of samples during processing/ annealing.

2.4 Hardness Measurement

Hardness was measured using MATSUZAWA Vickers Innovative Automatic (VIA)—S Tester perpendicular to the build direction. A load of 2 kg–f was applied on all the samples for a dwell time of 10 s.

2.5 Tensile Test

A tensile test performed by applying the load was applied perpendicular to the built direction according to ASTM E8 M. The surfaces of the fractured samples were observed using Secondary Electron (SE) mode in the SEM. Morphologies such as cracks, pores, dimples and voids were observed, and the mode of fracture was identified.

3 Results and Discussion

3.1 Microstructure

3.1.1 Microstructure in the As-Built Condition

Figure 1a and b show SEM micrographs of the as-fabricated Ti-6Al-4V sample at lower and higher magnifications, respectively. They reveal a fine α' martensitic structure,

Table 1 Chemical composition of the Ti-6Al-4V alloy powder

Element	Al	V	O	N	C	H	Fe	Y	Other elements	Ti
%Weight	5.5–6.75	3.5–4.5	0.2	0.05	0.08	0.015	0.3	0.005	0.4	Balance

Fig. 1 SEM Micrograph of the Ti-6Al-4V as-built samples revealing fine acicular martensitic α', unmelted particles and pores **a** low magnification, **b** high magnification
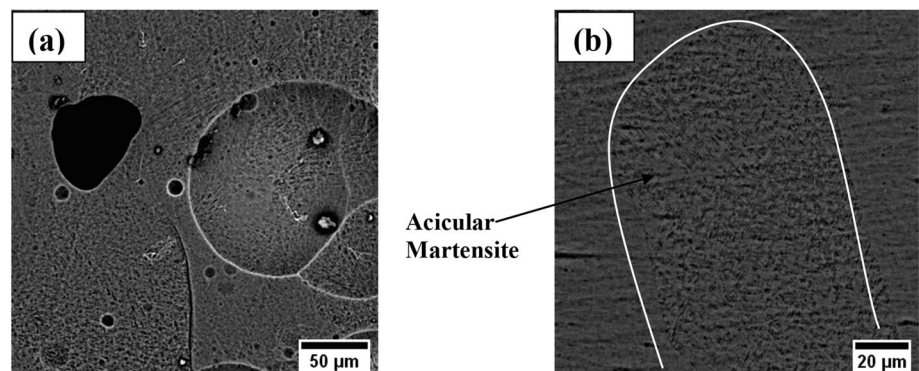
unmelted powder particles and pores. The fine α' martensitic structure is observed due to the high cooling rate in the SLM process. The spherical pores are due to gas entrapment during the SLM process, and the irregular-shaped pores are a result of insufficient fusion due to insufficient heat input.

3.1.2 The Effect of Annealing Temperature on Microstructure

Figure 2a–d show the optical microstructures of SLM printed Ti-6Al-4V samples annealed at 800 °C, 1000 °C, 1200 °C and 1400 °C. Sample annealed at 800 °C exhibits α grains in α + β matrix. Since the cooling rate is low and the annealing temperature is lower than the β transus temperature, the α' structure in the built condition is transformed into α + β structure through α nucleation and its growth process from prior β grain boundaries as shown in Fig. 2a. The grains are mostly near-equiaxed in shape. However, samples annealed at and above 1000 °C reveal the lamellar morphology (see Fig. 2b–d). The microstructure of SLM Ti-6Al-4V annealed near β transus temperature, i.e., 1000 °C, is shown in Fig. 2b. It displays prior β, inter-granular α and β lamellae.

With an increase in annealing temperature above 1000 °C, an increase in average α lamellar width and inter-granular β thickness is observed (see Fig. 2c and d). A significant increase in grain size is noticed for samples annealed above β transition temperature. Samples annealed at and above the β transus temperature display basket-weave morphology (since some α plates originate inside β grains rather than grain boundaries) and some non-lamellar regions.

All the samples have been found to have unmelted spherical/irregular particles of different sizes.

Figure 3a–d show the SEM micrographs of the annealed SLM samples at various temperatures. Pores, unmelted and partially melted particles of different sizes, can be seen in all the samples and porosity is decreased in all the annealed samples. Especially in the as-fabricated condition, a large number of unmelted particles and pores are seen, which implies that the energy input used in the current study might not have been sufficient to melt the particle completely. The chemical analysis of pores through EDS and unmelted particles shows the oxidation of AM Ti-6Al-4V at high annealing temperatures (see Fig. 3) despite the inert gas flow into the tubular furnace. In addition, the oxygen content is observed to be more in pores than in partially unmelted particles. This oxygen appears due to its low melting temperature and stochastic flow trend during SLM [28].

3.1.3 The Effect of Heat Treatment Temperature on Porosity and Grain Size

The volume fraction and relative density of the pores with respect to the annealing temperature are shown in Table 2. Samples annealed at 1000 °C show a much lower volume percentage of pores than other annealed samples, and a similar trend is observed in the density variation of the samples (standard density is considered to be 4.41 g/cc). The volume fraction of pores in the as-built condition is very high, i.e., 3.67%. The initial decrease in porosity owes to the vacuum

Fig. 2 Optical Microstructures of SLM printed Ti-6Al-4V samples annealed at **a** 800 °C **b** 1000 °C **c** 1200 °C **d** 1400 °C
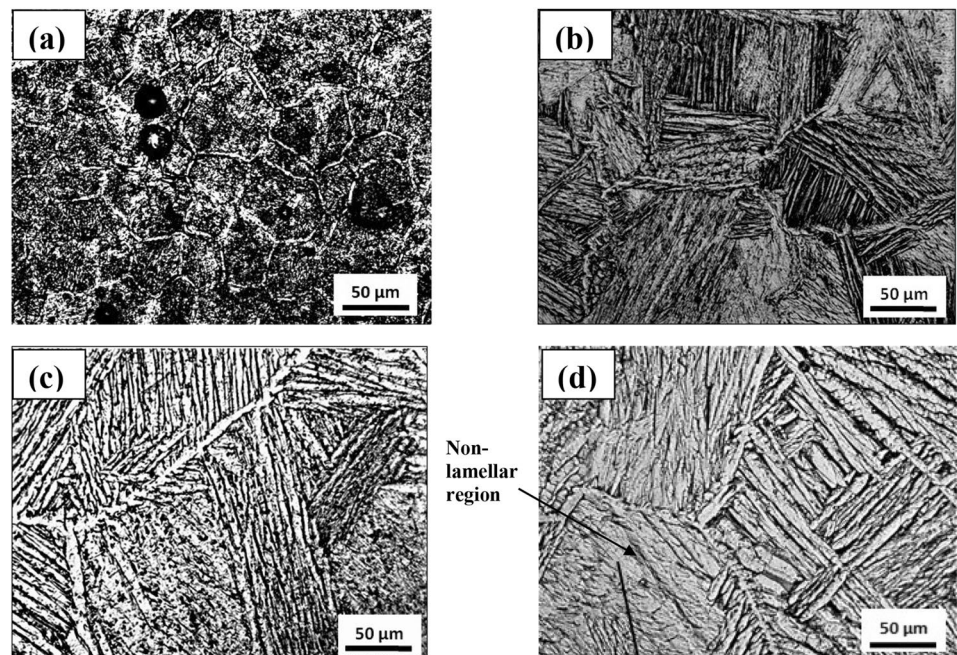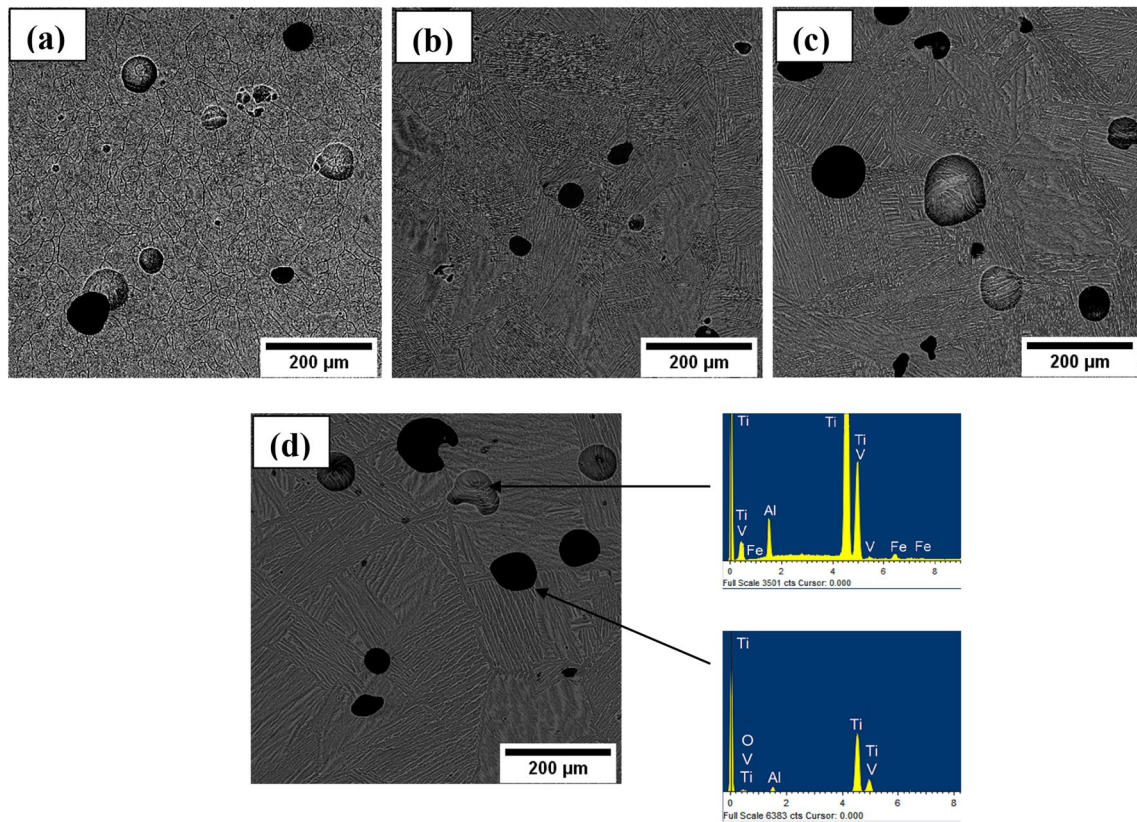
Fig. 3 SEM Micrographs of SLM Ti-6Al-4V samples annealed at **a** 800 °C **b** 1000 °C **c** 1200 °C **d** 1400 °C with EDS spectra of condition

Table 2 The density and porosity of as-SLMed and annealed samples

Annealing temperature (°C)	Density (g/cc)	Relative density (%)	Porosity (Vol %)
As-built	4.25	96.33	3.67
800	4.37	99.18	0.82
1000	4.41	99.99	0.01
1200	4.33	98.08	1.92
1400	4.33	98.13	1.87

atmosphere inside the tubular furnace and the pressure difference inside the sample and vacuum which must have eliminated the gas porosity due to Ar and O_2. Leuders S. et al. explained that the presence of Argon in the furnace rather than vacuum might impede the full closure of pores in the furnace during annealing treatment [29]. The re-growth of porosity in samples annealed above 1000 °C is analogous to the situation observed in Hot Isostatic Pressing of SEBM Ti64, where the high internal pressure of Ar induced during SLM after HIP was the driving force for the increase in porosity after a specific annealing temperature [30]. In the current study, the thermal stresses during SLM might

have been sufficiently high. Moreover, with an increase in annealing temperature beyond 1000 °C, pressure increases inside the furnace and, consequently, on the sample since the sample volume is constant. The above two criteria, when combined, can explain the high exerted pressure and retention of Ar entrapment in the sample, causing porosity when annealed at 1200 °C and 1400 °C. Besides Ar, the high oxygen in the samples annealed at high temperatures can also lead to increased porosity following the abovementioned mechanism.

The annealing temperature had a significant influence on grain morphology. Near-equiaxed grains were formed at low temperatures, whereas lamellar and basket weave morphologies within huge prior β grains were observed in high-temperature annealed samples. The grain size of the sample annealed at 800 °C is about 50 μm, and it is 3 times ($\sim$150 μm) more at 1000 °C. Then the grain size drastically increased to about 6–7 ($\sim$300–350 μm) times at 1200 °C and 1400 °C. This behaviour is due to $\alpha + \beta$ microstructure trying to hinder grain growth near the β transition temperatures.

A great increment in the average thickness of prior β boundaries, α lamellae and inter-granular β are also seen with annealing temperature (Fig. 4). In each case, the average α lamellar thickness is almost double the inter-granular
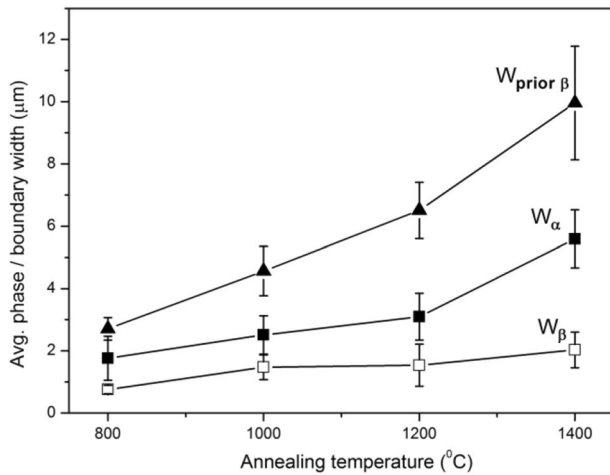
Fig. 4 The variation of phase/boundary thickness with respect to annealing temperature
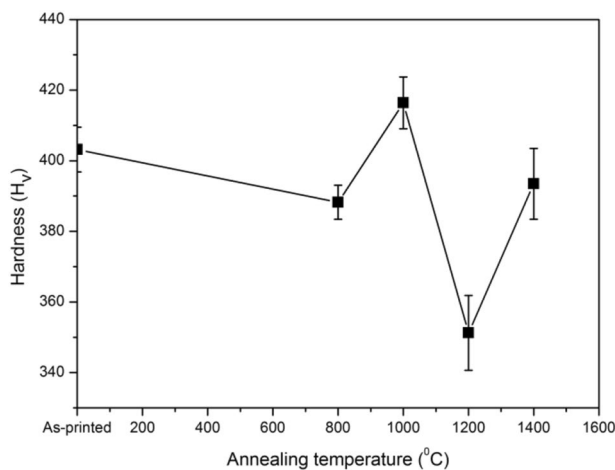
Fig. 5 The variation of hardness with annealing temperature

β width. However, after the β transus temperature, the latter is slightly increased, and no significant change is observed up to 1200 °C. From 1200 to 1400 °C, it increased slightly as compared to substantial increases observed in the width of lamellar α and prior β boundary. It can be inferred that, as the annealing temperature increased from $\alpha + \beta$ phase field to β field, the amount of β which transformed to lamellar α increased. Since a rise in temperature leads to increased diffusion rates and hence the growth rates, the α nuclei formed on prior β grain boundaries have grown to become larger plates.

3.2 Mechanical Properties

3.2.1 Hardness Measurement

The hardness variation with annealing temperature shows an irregular and unconventional trend (Fig. 5). In the as-built condition, the hardness is about 400 H_v. The high cooling rate or the lack of diffusion as a driving force led to a very fine α' acicular martensitic structure with high hardness. Then, a decrease in hardness is observed when annealed at 800 °C due to the nucleation and growth of the β phase and its subsequent conversion to α during annealing. Surprisingly, there is an increase in hardness at 1000 °C (416 H_v). The hardness is even greater than that observed in the as-SLM condition, although marginally. This can be explained by the comparatively low porosity in the sample annealed at 1000 °C. The substantial decrease in hardness from 1000 to 1200 °C can be attributed to the significant increase in grain size, average α lamellar thickness and porosity (~2%). *In addition, the micro-flow of residual powder particles with lighter mass can occur on the lateral surfaces due to gravity, which is a function of the temperature profile at the surface* [28]. *Further, the increase in hardness from 1200 to 1400 °C annealed samples can possibly be due to the slight decrease in porosity observed from 1.92 to 1.87%.* The unusual variation in hardness is similar to the trend followed by porosity with annealing temperature, which implies that porosity plays a major role in determining the hardness of SLM Ti64. This sensitivity of hardness to small changes in porosity/relative density is also observed by Khorasani et al. [28]. *However, the strength did not follow the same trend as hardness with the relative density, similar to our case.*

3.2.2 Tensile Properties

In the as-built condition, Ti-6Al-4V has a superior Yield strength (YS) and tensile strength (UTS), as seen in Fig. 6. This is because of the martensitic structure produced. Since fine acicular martensite is strong and brittle in nature, the values of YS and UTS are not only high but close to each other.

Among the annealed samples, YS and UTS are the highest at 800 °C. This is because of the hard and near-equiaxed α phase in the β matrix. Beyond 800 °C, both YS and UTS decreased until 1000 °C. Nevertheless, at 1200 °C and 1400 °C, there is not much difference in UTS, which is almost the same as that at 1000 °C, though, on the contrary, a continuous increase in average α lath thickness and β phase fraction is observed.

This initial decrease in strength with an increase in annealing temperature can be explained by three different factors: (1) since there is an increase in grain size with respect to the annealing temperature, from the Hall–Petch
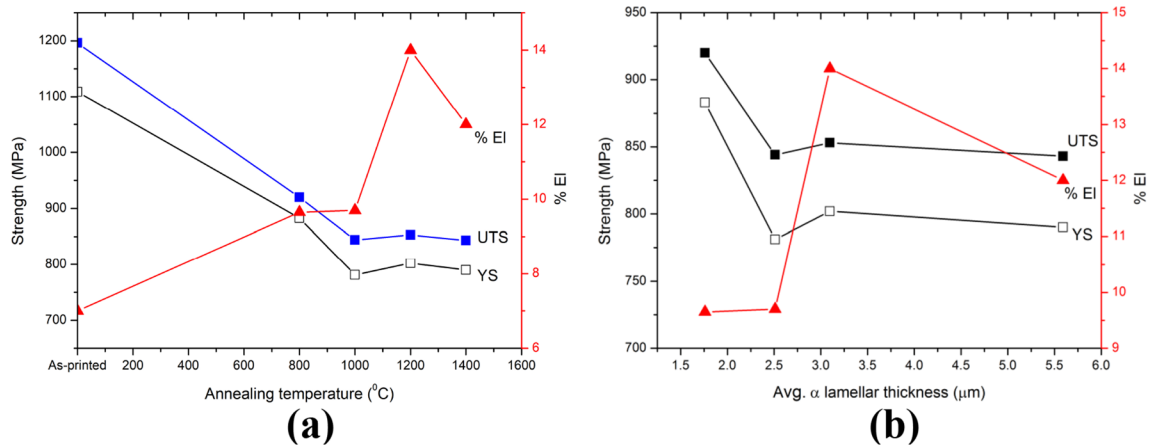
Fig. 6 Mechanical Properties at different **a** annealing temperatures **b** α lamellar thickness for annealed samples

relationship, there should be a considerable decrease in strength, (2) the volume fraction of the β increases when annealing temperature ≥ 1000 °C and β being the soft phase decreases the strength, (3) when annealed above β transus temperature, lamellar Widmanstatten structure is formed. In general, higher annealing temperature corresponds to higher α lath thickness [27]. Although strength and ductility follow this similar trend in Fig. 6a, they did not strictly decrease.

The % elongation for the as-fabricated sample is less compared to other samples. A steady increase in % elongation is observed with increasing annealing temperatures up to 1000 °C. Above 1000 °C, the effect of increase in grain size and average α lamellar thickness in improving the ductility is more pronounced than the ductility deterioration caused by the high porosity effect, which is reflected in the ductility increase by a value of 4% at 1200 °C. However, the sudden drop in ductility from 1200 to 1400 °C could be a result of deviation in β volume fraction intertwined with the distribution of Ti and V in α and β phases and differences in average pore size and shape.

Figure 6b displays the variation of mechanical properties with respect to average α lath thickness in annealed samples. The points represent annealed samples at 800 °C, 1000 °C, 1200 °C and 1400 °C (from left to right). Until an α lamellar width of 2.51 ± 0.62 μm (at 1000 °C), the strength decreased while the ductility increased slightly. The dramatic change in elongation in the sample annealed at 1200 °C is expected due to an increase in α lath thickness by ~ 0.7 μm, as discussed above. On the contrary, with an increase in annealing temperature from 1200 to 1400 °C, a reduction in elongation of $\sim 2\%$ might correspond to the dominance of distortion in the geometry of pores and phase volume fractions over increased α lath thickness as aforementioned. YS, UTS and % elongation follow a similar trend with respect to intergranular β thickness.

In the results, annealing at β transition temperature notably decreased the porosity but did not contribute to the increase in strength of the alloy beyond that of as-fabricated condition, albeit the highest hardness was observed in the sample annealed at 1000 °C. This disparity in strength and hardness values is unconventional from the established relationships that strength proportionately increases with hardness.

Table 3 compares the mechanical properties of the as-built samples in the current study to those processed by SLM using different process parameters/conditions in the literature. Xu Y. et al. implemented favourable conditions to control the temperature profile throughout SLM with the help of process parameters like laser energy density and the ratio of areas of the support structure to the built sample [10].

Vrancken B. et al. performed various heat treatments below the β transus temperature using furnace, air and water cooling regimes on SLM—printed Ti-6Al-4V samples and achieved the best mechanical properties in furnace cooling and air cooling-tempering cycle. [31].

Table 3 The Comparison of mechanical properties in as-fabricated condition with reference SLM studies on Ti-6Al-4V

Sample condition	Yield strength (MPa)	Ultimate tensile strength (MPa)	% Elongation
SLM (as-fabricated)	1109	1196	7
SLM (as-fabricated) [10]	~1141	~1241	6–7
SLM (as-fabricated) [31]	1110	1267	7.28
SLM (as-fabricated) [32]	1137	1206	7.6
SLM (as-fabricated) [33]	1156	1228	8.6

Vilaro T. et al. made a comparative study between as-cast, wrought and SLM-treated Ti-6Al-4V [32]. Though scanning strategy changes and process optimization resulted in a better ductility of SLM printed samples, Vilaro T. et al. argued that the properties would not be superior to conventional Ti-6Al-4V alloy unless defects could be completely avoided. Liang Z. et al. discussed how the microstructure evolution varies with factors such as the orientation of the sample and type of post-processing/heat treatment temperature and observed the finest α lamellae at 800 °C and 850 °C [33].

The values of strength in our results are comparatively lower since unmelted particles and pores played a crucial role in determining the mechanical properties.

Though all the samples are approximately greater than 98% dense, the defects have a significant impact on lowering the strength as well as ductility of SLM fabricated Ti-6Al-4V. Reducing the laser power during SLM, choosing a smaller layer thickness and a higher laser power during processing could possibly alleviate the retention of unmelted particles.

3.2.3 Fractography Analysis

Fractography analysis of the as-built sample shows the presence of cleavage facets and a small number of dispersed dimples (Fig. 7a), suggesting that the fracture is both ductile and brittle due to ~ 7% ductility. Figure 7b–e display the

Fig. 7 Fractographs of SLM Ti-6Al-4V **a** as-built condition, annealed at **b** 800 °C **c** 1000 °C **d** 1200 °C **e** 1400 °C
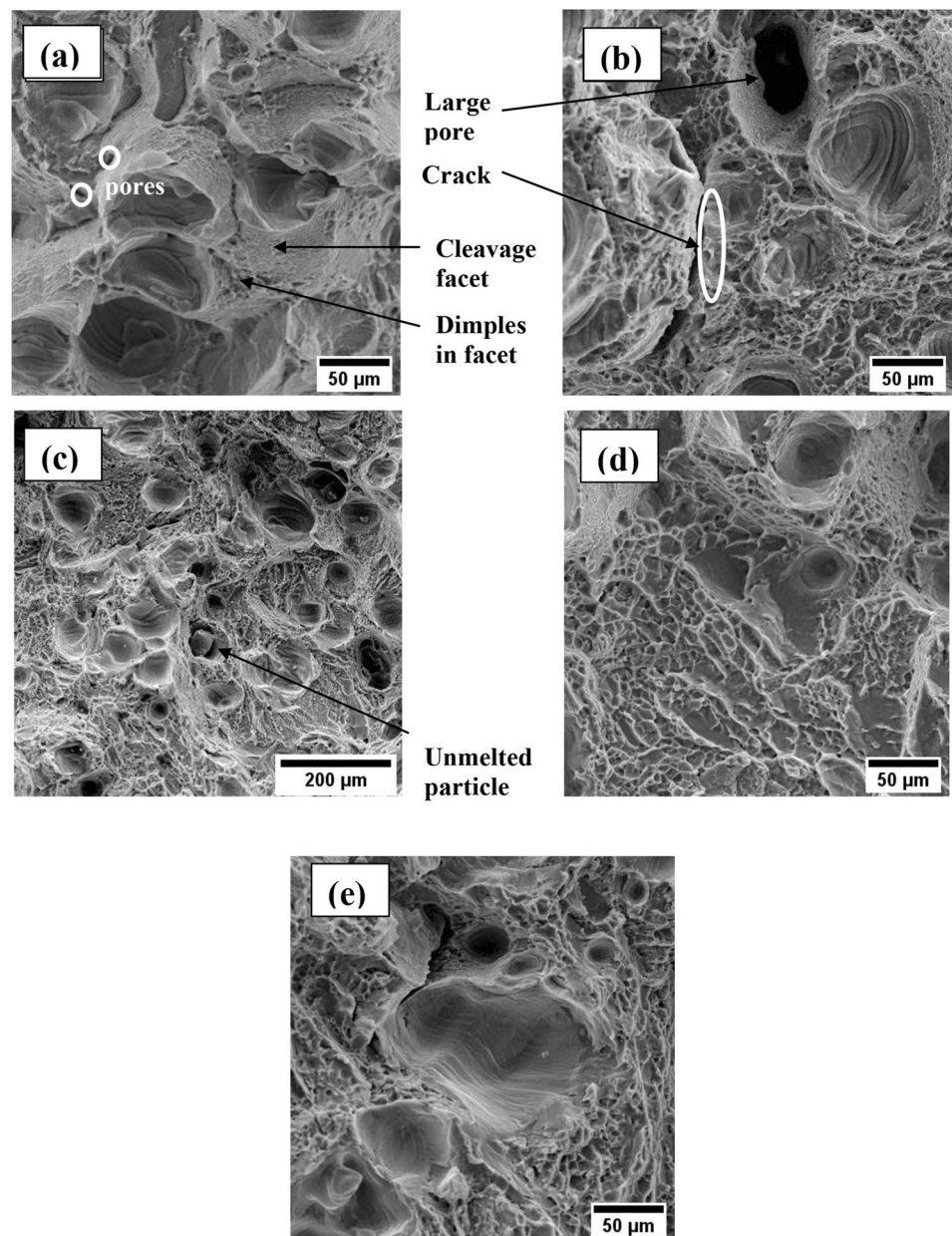
fractured surfaces of the annealed samples. All the images show the occurrence of a mixed mode of fracture, with pores mostly observed in the α phase.

A detailed analysis of the fractography results leads to a deeper comprehension of the observed mechanical properties. Leuders S. et al., in [29] noted the role of porosity and its potential effects on crack initiation and subsequent fatigue properties. In the present study, small pores indicated by the oval in Fig. 7a act as crack initiation sites. In cases where porosity is lower, especially in the sample annealed at 1000 °C, the slip pertains to the hcp α phase and the crack is generated in both equiaxed and lamellar α in areas where slip is localized. But the crack initiation at pores is relatively easier than at α phase due to more surface energy of atoms at the pore. Since porosity is more in the as-fabricated sample, the crack initiation sites would be more and give rise to fracture quickly, primarily producing facets during fracture even though the fracture can be classified as mixed mode. At 800 °C, 1000 °C, 1200 °C and 1400 °C, the fracture is mainly ductile and in agreement with the general trend in mechanical properties observed.

4 Conclusion

- The microstructure of as-built Ti-6Al-4V consisted of a combination of fine martensite (α'), unmelted particles and pores. Samples annealed below the β transus temperature revealed near-equiaxed α grains in α + β matrix, and samples annealed above β transus revealed the characteristic Widmanstatten structure.
- The highest amount of unmelted particles/porosity was found in the as-built sample, and the lowest was in the sample annealed at 1000 °C.
- The initial decrease in porosity and its subsequent increase could be attributed to the pressure difference between vacuum and Ar in the sample induced during SLM due to thermal stresses and increased pressure at high annealing temperatures on the sample, which can lead to gas entrapment, respectively. *The high oxygen found in high-temperature annealed samples would further increase the porosity due to the same reason as in the case with Ar.*
- EDS analysis confirmed the presence of oxygen in the annealed samples and the amount of oxygen increased on increasing the annealing temperature.
- The grain size and the average thickness of α lamellae, inter-granular β and prior β grain boundary increased with annealing temperature.
- The hardness (and ductility) values strongly depended on porosity while strength did not follow a similar trend. The sharp decrease in hardness of the sample annealed at 1200 °C was caused by the increase in grain size, α lath thickness and porosity. Micro-flow phenomenon at high temperatures could have been contributed to this decrease. The increase in hardness in 1400 °C annealed sample could be due to the slight decline in porosity which could have a significant effect.
- The strength decreased, and ductility increased due to an increase in slip length, grain size and β volume fraction. These effects dominated the increase in strength due to a decrease in porosity. In the sample annealed at 1200 °C, the high ductility observed was largely due to the ~ 0.7 µm increment in average α lath size. The reduced ductility at 1400 °C was anomalous and could be ascribed to the distortions in volume fraction of α and β and pore geometry.
- The as-built sample showed a very high strength due to the presence of acicular martensite. The sample annealed at 800 °C provided the optimum mechanical properties.
- The fractured surfaces of all the annealed samples showed a mixed mode of fracture, but the fracture was predominantly brittle in the as-built condition and ductile in the annealed conditions. The cracks were primarily generated from pores and the α phase.

References

1. Neikter M, Åkerfeldt P, Pederson R, and Antti M-L, *IOP Conf Series: Mater Sci Eng* **258**, (2017) 012007
2. Hong S Y, Ding Y, and Jeong W, *Int J Mach Tools Manuf* **41** (15), (2001) 2271–2285.
3. Jerold B D, and Kumar M P, *ASME J Manuf Sci Eng* **135** (3), (2013) 031005
4. Sivalingam V, Sun J, Yang B, Liu K, and Raju R, *J Manuf Process* **36**, (2018) 188–196.
5. Chetan Ghosh S, and Venkateswara Rao P, *J Cleaner Prod* **100**, (2015) 17–34.
6. Singaravel B, Shekar K C, Reddy G G, et al., *Ain Shams Eng J* **11** (1), (2019) 143–147.
7. Liu S, and Shin Y C, *Mater Design* **164**, (2019) 107552
8. Ngo T D, Kashani A, Imbalzano G, Nguyen K T Q, and Hui D, *Compos Part B: Eng* **143**, (2019) 172–196.
9. Li N, Huang S, Zhang G, Qin R, Liu W, Xiong H, and Blackburn J, *J Mater Sci Technol* **35** (2), (2018) 242–269.
10. Xu Y, Zhang D, Guo Y, Hu S, Wu X, and Jiang Y, *J Alloys Compd* **816**, (2020) 152536
11. Xu W, Brandt M, Sun S, Elambasseril J, Liu Q, Latham K, and Qian M, *Acta Mater* **85**, (2015) 74–84.
12. Simonelli M, Tse Y Y, and Tuck C, *J Mater Res* **29** (17), (2014) 2028–2035.

13. Malý M, Höller C, Skalon M, Meier B, Koutný D, Pichler R, and Paloušek D, *Materials* **12** (6), (2019) 930.

14. Al-Rubaie K S, Melotti S, Rabelo A, Paiva J M, Elbestawi M A, and Veldhuis S C, *J Manuf Processes* **57**, (2020) 768–786.

15. Simonelli M, Tse Y Y, and Tuck C, *Mater Sci Eng: A* **616**, (2014) 1–11.

16. Zhou B, Zhou J, Li H, and Lin F, *Mater Sci Eng: A* **724**, (2018) 1–10.

17. Liu L, Chen C, Zhao R, Wang X, Tao H, Shuai S, and Ren Z, *Addit Manuf* **46**, (2021) 102142

18. Yang J, Yu H, Yin J, Gao M, Wang Z, and Zeng X, *Mater Design* **108**, (2016) 308–318.

19. Do D K, and Li P, *Virt Phys Protot* **11** (1), (2016) 41–47.

20. Liu J, Sun Q, Zhou C, Wang X, Li H, Guo K, and Sun J, *Mater Sci Eng A* **766**, (2019) 138319

21. Song B, Dong S, Liao H, and Coddet C, *Int J Adv Manuf Technol* **61** (9–12), (2011) 967–974.

22. Manvatkar V, De A, and DebRoy T, *Mater Sci Technol* **31** (8), (2014) 924–930.

23. Sun J, Yang Y, and Wang D, *Optics Laser Technol* **49**, (2013) 118–124.

24. Shi X, Ma S, Liu C, Chen C, Wu Q, Chen X, and Lu J, *Materials* **9** (12), (2016) 975.

25. Shao M, Vijayan S, and Jinschek J, *Microsc Microanal* **27** (S1), (2021) 2682–2684.

26. Gong H, Rafi K, Gu H, Janaki-Ram G D, Starr T, and Stucker B, *Mater Des* **86**, (2015) 545–554.

27. Zhang X-Y, Fang G, Leeflang S, Böttger A J, Zadpoor A, and Zhou J, *J Alloys Compd* **735**, (2018) 1562–1575.

28. Khorasani A M, Gibson I, Awan U S, and Ghaderi A, *Addit Manuf* **2019** (25), (2019) 176–186.

29. Leuders S, Thöne M, Riemer A, Niendorf T, Tröster T, Richard H A, and Maier H J, *Int J Fatigue* **48**, (2013) 300–307.

30. Tammas-Williams S, Withers P J, Todd I, and Prangnell P B, *Scripta Materialia* **122**, (2016) 72–76.

31. Vrancken B, Thijs L, Kruth J-P, and Van Humbeeck J, *J Alloys Compd* **541**, (2012) 177–185.

32. Vilaro T, Colin C, and Bartout J D, *Metall Mater Trans A* **42** (10), (2011) 3190–3199.

33. Liang Z, Sun Z, Zhang W, Wu S, and Chang H, *J Alloys Compd* **782**, (2019) 1041–1048.